NJC

PAPER

View Article Online
View Journal | View Issue

Cite this: *New J. Chem.*, 2023, **47**, 1105

Improving catalytic performance *via* induction heating: selective oxidation of H_2S on a nitrogen-doped carbon catalyst as a model reaction

Wei Wang,[a] Cuong Duong-Viet,*[ab] Lai Truong-Phuoc,[a] Tri Truong-Huu,[c] Hoang M. Nguyen,[c] Lam Nguyen-Dinh,[c] Yuefeng Liu[d] and Cuong Pham-Huu*[a]

Received 4th October 2022,
Accepted 30th November 2022

DOI: 10.1039/d2nj04897c

rsc.li/njc

In this work, a macroscopic nitrogen-doped mesoporous carbon-coated silicon carbide catalyst (NMC/SiC) was developed and fully evaluated as a metal-free catalyst for the selective oxidation of H_2S into elemental sulfur under various conditions using both noncontact induction heating (IH) and classical Joule heating (JH) modes. The results obtained indicated that the coated SiC catalyst exhibited excellent desulfurization performance when operated with induction heating. Indeed, when operated with IH, the catalyst displays better desulfurization performance under challenging reaction conditions, *i.e.*, a low reaction temperature of 180 °C and a high gaseous space velocity of 3600 h^{-1}, than when operated using the indirect convection/conduction JH mode. The high desulfurization performance was attributed to the highly effective heat management inside the catalyst bed *via* an IH along with a short diffusion length associated with the nanoscopic dimension of the nitrogen-doped carbon coating layer on the macroscopic silicon carbide host substrate. The catalyst also displays high stability as a function of time on stream thanks to the high stability and activity of nitrogen sites.

1. Introduction

The improvement in catalysis field stems from the development of new and optimized catalysts as well as catalytic processes with better energy efficiency in order to reduce as much as possible the associated carbon footprint of the process. The increasing awareness of climate changes and the still too slow decarbonization of our industrial society have triggered scientists to develop new chemical processes, thereby making them less and less dependent on fossil resources.[1,2] Induction heating (IH) has been widely developed in the manufacturing of industrial metallic work pieces (bonding, welding, and sintering) in several industries.[3,4] This heating approach enables us to generate heat directly inside the targeted materials, and thus, significantly reduces the energy waste caused by heat conduction and/or radiation usually observed with the conventional heating mode. With this technology, heat can be directed to the predefined region without over heating the whole large zone as well as the gas phase reactant. Therefore, it can avoid thermal decomposition of reactants or intermediate compounds caused by overheating of the whole reactor.[5,6] Recently, the IH mode has been reported as an efficient heating mode for operating catalytic processes with significantly improved performance.[6–11] Besides the above-mentioned advantages, IH represents a green heating means for operating catalytic processes, as it can be operated using exceeding renewable electricity, instead of using a traditional fuel burner for providing heat to the reactor, which contributes to the reduction of CO_2 for the process.[6,12,13]

Hydrogen sulfide (H_2S), one of the major toxic and malodorous gases, is commonly emitted from chemical industries, such as natural gas refineries, crude oil, biogas purification and coal chemistry. H_2S is not only harmful to humans but also induces corrosion in the facilities and pipeline as well as downstream catalyst poisoning.[14–16] The most widely method for removing H_2S is the equilibrated Claus process ($2H_2S + 3O_2 \rightarrow 2SO_2 + 2H_2O$ and $4H_2S + 2SO_2 \rightarrow 3S_2 + 4H_2O$). However, there is still 3–5% H_2S remaining in the tail gas due to the thermodynamic limitation, which is higher than the standard of legislation requirements for the discharge of the off-gas into the atmosphere. The catalytic selective oxidation process ($2H_2S + O_2 \rightarrow (2/n)S_n + 2H_2O$), in which H_2S can be directly oxidized into elemental sulfur by

[a] *Institute of Chemistry and Processes for Energy, Environment and Health (ICPEES), ECPM, UMR 7515 of the CNRS and University of Strasbourg, 25 rue Becquerel, 67087 Strasbourg Cedex 02, France. E-mail: duongviet@unistra.fr, cuong.pham-huu@unistra.fr*
[b] *Ha-Noi University of Mining and Geology, 18 Pho Vien, Duc Thang, Bac Tu Liem, Ha-Noi, Vietnam*
[c] *Department of Chemical Engineering, The University of Da Nang – University of Science and Technology, Da Nang 550000, Vietnam*
[d] *Dalian National Laboratory for Clean Energy (DNL), Dalian Institute of Chemical Physics, Chinese Academy of Science, 457 Zhongshan Road, 116023 Dalian, P. R. China*

oxygen, has attracted tremendous attention due to its low cost, high efficiency and non-thermodynamic process.[17–20] Over the past few decades, many groups have developed metal-free catalysts based on the nitrogen-doped nanocarbon materials for H_2S selective oxidation in terms of microstructure design,[21–23] nitrogen contents and species regulation,[24–27] alkali promotion[28–30] as well as the monolithic structure fabrication.[31–34] Most importantly, the superior thermal-/electro-conductivity properties over carbon-based materials make it the promising catalyst or catalyst support under IH model reactions.[35,36] Recently, Truong-Huu *et al.*[36] first reported that a macroscopic shaped carbon nanotube/carbon fiber monolith with abundant surface oxygenate groups has superior activity in the H_2S oxidation reaction under the IH model.

To achieve an efficient catalyst system by using the IH model for the selective oxidation of H_2S, a well-designed nitrogen-doped mesoporous carbon-coated industrial silica carbide catalyst (NMC/SiC) was applied and experimental parameters such as gaseous space velocity, reaction temperature and O_2/H_2S molar ratio were carefully investigated. It is worthy to note that porous SiC was chosen for supporting NMC active sites as it possesses all the properties required for a catalyst support, namely, high mechanical strength, high thermal conductivity which allow rapid homogenization of the temperature within the catalyst bed, high oxidative resistance and chemically inertness.[37,38] It is expected that the real on-time temperature regulation capability of the IH system could allow us to carry out the catalytic process under more drastic reaction conditions, *i.e.*, a low temperature and a high gaseous space velocity (GHSV), which could significantly impact the conversion level, compared to the traditional indirect JH mode, without noticeable loss in terms of catalytic performance due to the high efficiency for maintaining the catalyst surface temperature. This finding could be applied not only to this model reaction but also to other catalytic reactions.

2. Materials and methods

2.1 Silicon carbide support

Porous silicon carbide (β-SiC) was produced *via* a gas–solid synthesis process[39] according to the following reaction equations (1) and (2):

$$SiO_2 + Si \leftrightarrow 2SiO \quad (1)$$

$$SiO + C \rightarrow SiC + CO \quad (2)$$

During synthesis, CO formed from the reaction (eqn (2)) was continuously flushed by an argon stream, which forces the displacement of the reaction shift towards the right side. The industrial process developed by SICAT Co. (**https://www.sicatcatalyst.com**) allows the production of β-SiC with a capacity of *ca.* 50 tons per year in different sizes and shapes depending on the downstream applications. The obtained β-SiC displays an exclusive meso- and macropore network, which renders it suitable for use as a medium thermal conductor support in numerous catalytic processes. It displays a total pore volume of 0.120 $cm^3\ g^{-1}$ and is mostly composed of mesopores with an average pore size distribution centered at around 12.8 ± 1.5 nm.

2.2 Synthesis of NMC/SiC monolith catalysts

Commercial β-SiC in the form of extrudates ($D \approx 1$ mm, $L \approx 3$ mm) was thoroughly washed with deionized water in order to remove powdery material fractions followed by complete drying at 130 °C overnight. The nitrogen-doped mesoporous carbon coating process has been widely reported in our previous studies.[31,40–42] In a typical procedure, 1.5 g of D-glucose and 2.25 g of citric acid were added into 10 mL of ultrapure Milli-Q water at room temperature. Afterwards, 1.73 g of ammonium carbonate was added in a single portion to this solution under slow stirring at room temperature and an instantaneous effervescence due to CO_2 evolution was observed. The obtained clear solution was subsequently impregnated onto 10 g of SiC dropwise. The impregnated wet solid was maintained at 40 °C until the surface was dried before heated up to 130 °C in air for 1 h. The as-synthesized composite was then annealed at 900 °C in He at a heating rate of 5 °C min^{-1} for 2 h, during which the mesoporous N-doped graphitized C-coating on the SiC matrix was formed. The digital photo of the pristine SiC is presented in Fig. 1A. The NMC/SiC support displays the same morphology and a darker color than that of the pristine SiC support (not shown), which could be attributed to the presence of the coated NMC layer.

The SEM and TEM micrographs in Fig. 1B and C evidence the highly porous structure of the SiC support, which is composed of small particles aggregated with each other to form a material matrix. The TEM micrograph shown in Fig. 1D highlights the SiC microstructure covered in part by a thin layer of oxidic phase, *i.e.*, SiO_xC_y/SiO_2, in an amorphous structure. The high-resolution TEM micrograph shown in Fig. 1E clearly evidences the presence of stacking faults along the (111) growth axis of the SiC material and the SiO_xC_y/SiO_2 amorphous on the topmost surface.

The anchorage of the NMC layer on the SiC support could be favored by the presence of a thin layer of SiO_xC_y/SiO_2 on the SiC surface,[37] which provided oxygenated functional groups for interaction with the NMC precursors. Indeed, the SiO_xC_y/SiO_2 layer is relatively thin, *i.e.*, 3–5 nm, which will not alter the intrinsic thermal conductivity of the ceramic support but just play a role as an anchorage interface for the deposited nitrogen-doped carbon layer. Previous results have shown that the SiC support significantly improved heat transfer *via* the catalyst bed due to its medium thermal conductivity, compared to the other insulator materials.[43]

2.3 Characterization techniques

Scanning electron microscopy (SEM) was carried out using a ZEISS 2600F microscope with a resolution of 5 nm. The sample was deposited onto a double-face graphite tape in order to avoid charging effect during the analysis. Transmission electron microscopic (TEM) analysis was carried out using a JEOL 2100F operating at 200 kV accelerating voltage, equipped with a probe corrector for spherical aberrations, and a point-to-point resolution of 0.2 nm. The sample was dispersed by ultrasound

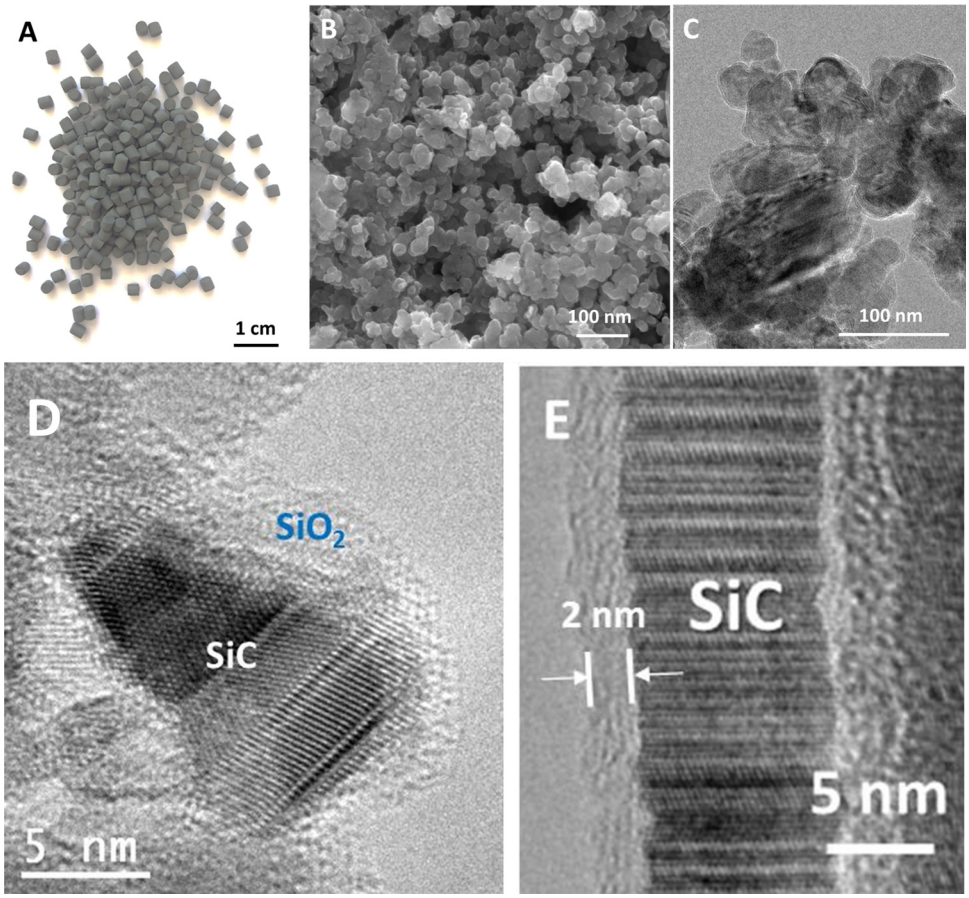

Fig. 1 (A) Digital photo of the pristine SiC support. (B) SEM micrograph of SiC showing the highly porous structure of the support. (C–E) Representative TEM and high-resolution TEM micrographs of SiC, with stacking faults along the [111] direction, covered with a thin hydrophilic passivated layer of SiO_xC_y/SiO_2 (with an average thickness of 2 nm).

in an ethanol solution for 5 minutes and a drop of the solution was deposited onto a copper plate covered with a holey carbon membrane for observation. The elemental mapping of different species, *e.g.*, Si (SiC), C (SiC), and N (NMC), was carried out by scanning transmission electron microscopy (STEM) using a JEOL 2100F electron microscope equipped with a Gatan Energy Filter and cold field-emission gun (FEG) operating at 200 kV with 1.5 Å lattice resolution. The Brunauer–Emmett–Teller (BET) specific surface area (SSA) and the pore size distribution of the support and the catalyst, after thermal treatment, were determined by liquid N_2-adsorption and desorption using an ASAP 2020 Micromeritics® instrument. All the samples were degassed at 250 °C under vacuum for 8 h in order to remove all the moisture. The pore size distribution was calculated from the desorption branch of the isotherm using the Barrett–Joyner–Halenda (BJH) approach. Thermal gravimetric analysis (TGA) was performed using a TGA Q5000 instrument at a heating rate of 10 °C min^{-1} under air flow in the atmosphere (20 mL min^{-1}). The weight of the sample was kept at around 10 mg in order to avoid diffusion problems during the analysis. Electrical conductivity of a cylinder filled with the catalyst extrudates and covered with two copper plates was tested using a 115 Fluke digital multimeter.

2.4 H_2S selective oxidation process

The H_2S oxidation process can be outlined according to main eqn (3)–(5):

$$H_2S + \tfrac{1}{2}O_2 \rightarrow 1/nS_n + H_2O \quad \Delta H = -222 \text{ kJ mol}^{-1} \quad (3)$$

$$S + O_2 \rightarrow SO_2 \quad \Delta H = -297 \text{ kJ mol}^{-1} \quad (4)$$

$$2H_2S + 3O_2 \rightarrow 2SO_2 + 2H_2O \quad \Delta H = -381 \text{ kJ mol}^{-1} \quad (5)$$

For conventional Joule heating, 6.0 g of NMC/SiC ($V_{cat.} \sim 7.5$ cm^3) was loaded on a silica wool pad located in a tubular Pyrex reactor (with an inner diameter of 26 mm) and housed in a vertical tubular electrical furnace. The furnace temperature was controlled by a K-type thermocouple and a Minicor regulator located next to the external wall of the reactor. The reactant gas mixture [H_2S (1 vol%), O_2 (2.5 vol%), H_2O (30 vol%) in inert He as a carrier (balance)] was passed downward through the catalyst bed. All the gas flow rates were monitored using Brooks 5850TR mass flow controllers. Steam (30 vol%) in the reactant feed was ensured by bubbling the inert carrier in a saturator containing hot water at 80 °C in order to simulate the industrial effluent. The gas hourly space velocity (GHSV) was fixed at 1200 and 3600 h^{-1} and the O_2-to-H_2S molar ratio was

evaluated ranging from 0.6 to 2.5. All catalytic runs were carried out in the continuous mode. Elemental sulphur was vaporized (because of the high partial pressure of sulphur at the reaction temperature) and condensed alongside with steam at the reactor outlet in a trap maintained at room temperature. The analysis of the inlet and outlet gases was performed on-line using a Varian CP-3800 gas chromatograph (GC) equipped with a Chrompack CP-SilicaPLOT capillary column and a thermal catharometer detector (TCD) for the detection of O_2, H_2S, H_2O and SO_2. H_2S and SO_2 concentrations were recalculated on the basis of the corrected flow after steam condensation. All the connecting lines were wrapped with thermal tapes and maintained at 140 °C in order to prevent any condensation.

The IH experiment was conducted using an EasyHeat® 8310 induction heating setup (10 kW, Ambrell Ltd) equipped with a spiral 6-turn induction coil (L = 1.05 m, pure coil resistance = 2.066×10^{-3} Ω) and an external cooling chiller with a recirculated water/glycerol (10%) mixture as a cooling medium. In a typical experiment, one glass reactor containing the catalyst, similar to that used for the JH, was placed inside the induction heater coils. The real-time temperature control/regulation was ensured using a PID system (Proportional Integral Derivative controller, Eurotherm model 3504) connected to a laser pyrometer (Optris®, power $<$ 1 mW, located at ≈30 cm from the catalyst) focused on the middle of the catalyst bed and with the capability of working in the 150–1000 °C range. The heating/cooling rate allowed for the system is about 300 °C min^{-1} in the 160–300 °C temperature range. The laser beam was focused on the extrudates constituting the catalyst bed localized behind the reactor wall.

It is worthy to note that the inductor was operated at a frequency of 263 kHz, which generated a much lower magnetic field than those generated at a lower frequency, *i.e.*, $<$10 kHz.[44,45] In addition, magnetic fields from low-frequency induction are more penetrating to the surrounding material. However, in order to reduce the exposure of the worker to the magnetic field, the setup was localized inside a Faraday cage surrounded with a metal mesh.

3. Results and discussion

3.1 Nitrogen-doped mesoporous carbon coated on SiC

The specific surface area (SSA) of the NMC/SiC significantly increases compared to that of the pristine SiC support despite the relatively low loading of the NMC phase (*ca.* 5 wt%), *e.g.*, 54 m^2 g^{-1} *vs.* 24 m^2 g^{-1}, which could be attributed to the micro- and mesoporous characters of the NMC phase according to our previous reports.[31,42] The coating of the SiC material with a layer of NMC also significantly modified the pore size distribution of the final composite with the contribution of small mesopores having an average pore size distribution centered at *ca.* 2.0 ± 0.5 nm. According to the results, the introduction of the nitrogen-doped carbon layer significantly modifies the overall porosity of the final composite. The detailed description of the catalyst characteristics can be found in our previous report.[42]

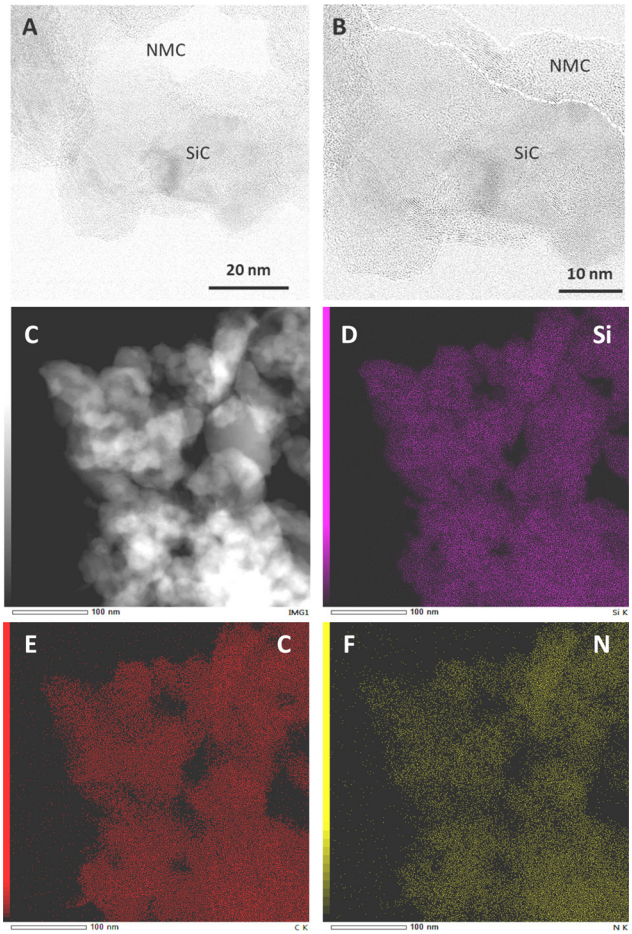

Fig. 2 (A and B) HR-TEM images of the NMC/SiC catalyst indicating the presence of a homogeneous and thin layer of NMC on the SiC support. (C–F) HAADF-STEM and EELS mapping images (Si, C and N elements) showing the coverage of the SiC support by the NMC layer.

The coating of the SiC support by a layer of NMC also increases the overall conductivity of the composite. An average resistance of 2000 kΩ was measured for the pristine SiC extrudates, while for NMC/SiC, the resistance value drastically drops to 12 kΩ, indicating the large improvement of the conductivity. These results confirmed the large difference between the surface NMC coating layer and the bulk support in terms of interaction with the magnetic field and, consequently, its respective surface temperature.

The HR-TEM images of the NMC/SiC catalyst are displayed in Fig. 2A and B. The amorphous nature of NMC is clearly visible on the surface of the SiC support. This amorphous and porous nitrogen-doped carbon layer is expected to offer a large surface area with abundant active sites to the reactants, leading to a significant improvement in the catalytic performance. It is also expected that this carbon layer could participate in the heat transfer throughout the whole catalyst body, and thus, reduce the formation of local hot spots inside the catalyst bed, which is detrimental to the selectivity. According to the results, the NMC layer was homogeneously coated onto the SiC host matrix surface with an average thickness of *ca.* 10 ± 2 nm.

The HAADF-STEM and EELS mapping images of the NMC/SiC catalyst (Fig. 2C–F) clearly confirm the homogeneous coating of the nitrogen-doped mesoporous carbon layer on the SiC surface according to the high overlap between the elemental signals of Si and N. Such a thin coating layer displays high accessibility for the reactant to the whole active phase, which is not the case for traditional supported catalysts, where some active sites are inevitably located far inside the pores of the support and cannot be fully accessible for the reactant, resulting in limited intrinsic activity. The uniformity of the NMC coating layer was also investigated by statistical STEM-EELS analysis on several areas of the catalyst (not shown), which confirms the homogeneity of the coating on the surface of the support. It is worthy to note that due to the extremely low thickness of the coating layer, the high-resolution TEM is the sole technique that allows us to access such coatings.

The TGA spectra of the pristine SiC support and the one coated with a layer of NMC are presented in Fig. 3A and B. Pristine SiC displayed a slight weight loss of *ca.* 3.2 wt% at a temperature of *ca.* 692 °C, which could be attributed to the combustion of some residual carbon localized within the materials (Fig. 3A). At a temperature higher than 700 °C, part of SiC was converted into SiO_2, leading to a gradual weight increase. The NMC-coated SiC sample displayed a weight loss at lower temperatures, *i.e.*, 612 *vs.* 692 °C, as shown in the TGA spectrum in Fig. 3B. The difference in terms of weight loss between the two samples allows us to calculate the NMC loading to *ca.* 5 wt%. The surface chemical composition of the SiC and NMC/SiC materials was analyzed by XPS, and the results are presented in Fig. 3C and D. According to the XPS Si_{2p} results (Fig. 3C), the SiC surface was composed of several Si species, which could be attributed to the presence of SiC and a mixture of SiO_xC_y/SiO_2 layer-coated SiC core,[37] while over the NMC/SiC sample, nitrogen species can be observed, *e.g.*, pyridinic, pyrrolic, quaternary and oxidized nitrogen species, according to the high-resolution N_{1s} spectrum (Fig. 3D).

3.2 H_2S selective oxidation

3.2.1 Influence of the reaction gaseous space velocity. In most of the catalytic processes, the ability of the catalyst to convert a large amount of reactants per time unit represents a main factor, as it will condition the size of the reactor for a given productivity of the plant. However, the catalytic performance is strongly influenced by the reactant gaseous space velocity, as it leads to a shorter contact time, which could impact the reactivity, and also an increase in the rate of heat removal *via* solid–gas exchange, which could lower the catalyst surface temperature and, in turn, the catalytic performance. In this section, the influence of the heating mode on the maintenance of the desulfurization performance, expressed in terms of H_2S conversion and SO_2 selectivity, as a function of the reactant gaseous hourly space velocity (GHSV) will be investigated, and the results are summarized in Fig. 4. The blank test carried out with a bare SiC support (not shown) confirmed the

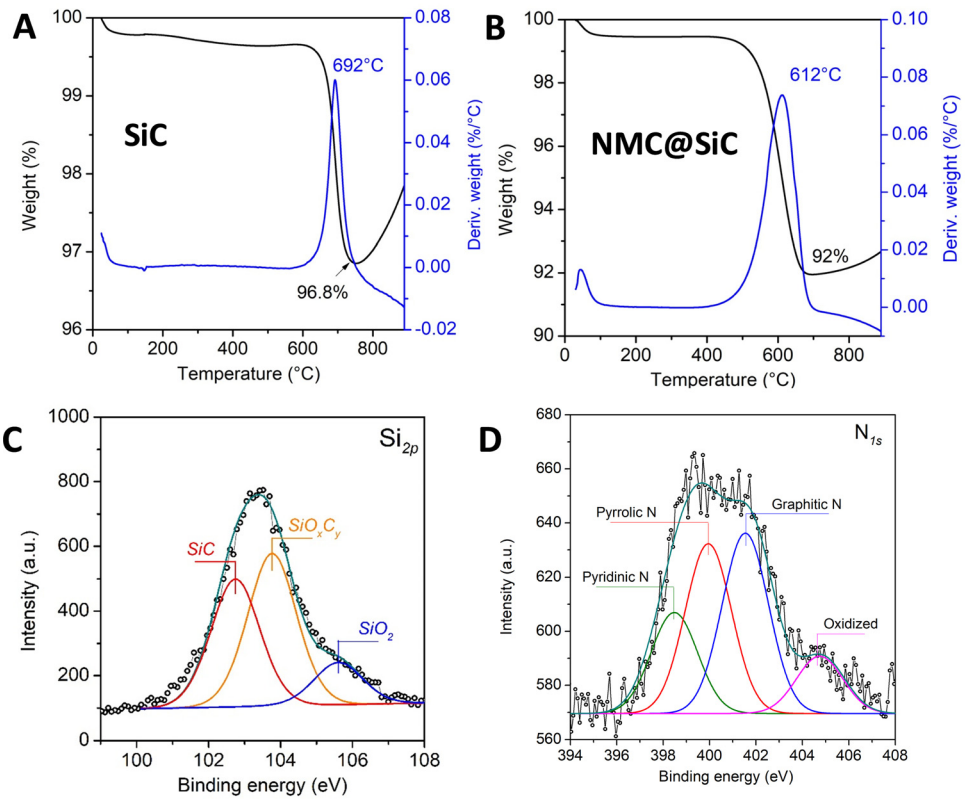

Fig. 3 TGA profiles of the (A) SiC and (B) NMC/SiC samples in air flow. (C and D) High-resolution XPS Si_{2p} and N_{1s} spectra of the NMC/SiC sample.

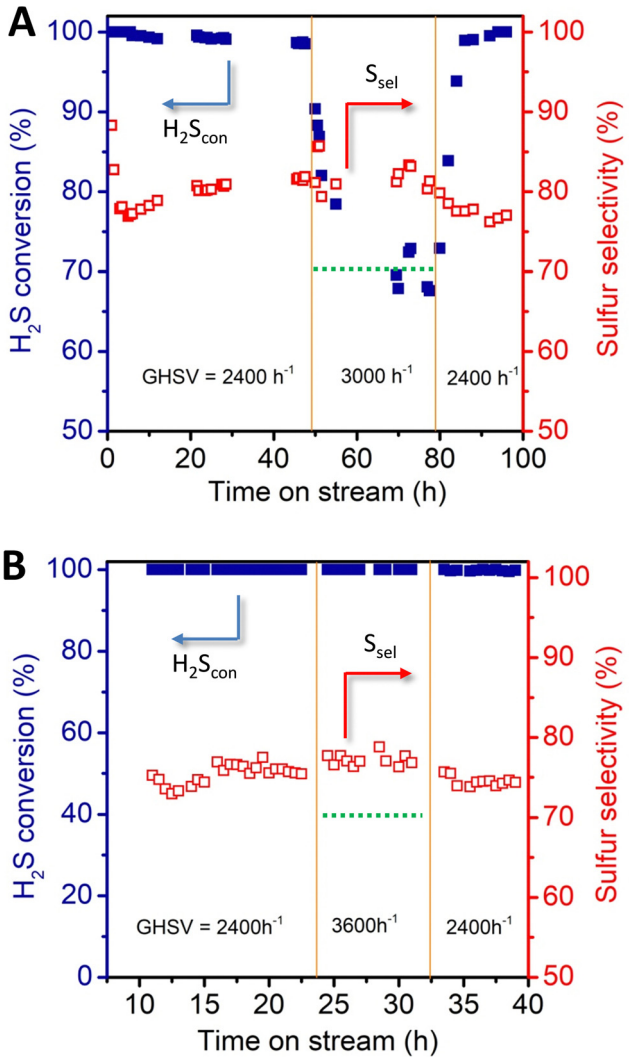

Fig. 4 Desulfurization performance on NMC/SiC operating under (A) JH and (B) IH. Reaction conditions: [H_2S] = 1 vol%, [O_2] = 2.5 vol%, [H_2O] = 30 vol%, O_2-to-H_2S ratio of 2.5, He (balance), 6.0 g NMC/SiC ($V_{cat.}$ ~ 7.5 cm^3), 210 °C.

complete inactivity of the support for the desulfurization process at different temperatures.

Under traditional Joule heating (JH), the thermal inertia of the oven is unable to achieve on real-time temperature compensation inside the catalyst bed caused by the increase in the GHSV, which leads to a net decrease in the catalytic performance, though no irreversible deactivation was observed according to the return test (Fig. 4A). Indeed, under the JH mode, increasing the GHSV, from 2400 h^{-1} to 3000 h^{-1}, leads to a significant decrease in H_2S conversion, from 98% to 70%, whereas the sulfur selectivity displays no obvious change. Similar results have also been reported on the monolithic carbocatalysts doped with different heteroelements, *e.g.*, N and P, as reported by Xu and co-workers.[34,46] However, it is expected that induction heating (IH) could be the heating mode of choice for operating the reaction under high reactant gaseous velocity, as the surface reaction temperature of the catalyst is adjusted constantly and rapidly by the inductor (only the catalyst was heated with the direct feedback of the catalyst temperature to the inductor setup), at a heating rate as high as several hundred degrees per minute. The results obtained at 2400 h^{-1} clearly indicated the better maintenance of the desulfurization performance on the NMC/SiC catalyst operated under the IH mode (Fig. 4B, left part). In order to verify such improvement in terms of catalytic performance, the reaction was carried out under a higher GHSV, *i.e.*, 3600 h^{-1} instead of 2400 h^{-1}, and the results are presented in Fig. 4B (center part). Unlike the results obtained under JH, the desulfurization of the NMC/SiC catalyst, operated under IH, remains at almost 100%, even under higher GHSV conditions, along with slightly improved sulfur selectivity. The return test back to a GHSV of 2400 h^{-1} restored completely the desulfurization performance and confirmed, as for the catalyst operated under the JH mode, that no deactivation occurred on the catalyst under different GHSV. The results obtained here definitively highlight the superiority of IH for operating catalytic processes on the NMC/SiC catalyst at a high space velocity.

The results obtained can be discussed as follows: it is expected that under IH regulation, the temperature variation on the catalyst surface, consecutive to the increase in the gaseous reactant velocity which induces higher gas–solid heat exchange, was rapidly regulated *via* fast heating adjustment, which thus, allows the maintenance of the reaction temperature and the desulfurization performance. A recent study by Malhotra *et al.*[47] on the heat behavior inside the catalytic reactor operated under selective and localized microwave heating has reported a similar fact about the influence of the reactant flow rate on the surface temperature of the catalyst. According to the simulation results, the reactant flow rate has almost no influence on the catalyst temperature under microwave heating as only the catalyst, with high response heating rate, was heated, while the reactant gas-phase entering the catalytic bed remains cold. As soon as the reactant gas entered the catalyst bed, which was maintained at the reaction temperature, the gas was heated up to the reaction temperature *via* rapid gas–solid heat exchange and the reaction starts.[48] However, the same simulation using indirect boundary heating, similar to the JH, where all the reactor length was heated to the same temperature, reveals that the gas-phase velocity induces a significant change in the catalyst temperature, at least at the entrance of the catalyst bed. Indeed, at a gaseous velocity fixed at 100 sccm, the catalyst temperature remains unchanged with respect to the set temperature, whereas, at a gaseous velocity of 1000 sccm, a large drop in temperature was observed at the entrance part of the catalyst, *ca.* 300 K below the set temperature, due to the decrease in the temperature at the entrance part of the reactor as the high flow cannot be heated up effectively and also to the high gas–solid temperature exchange. The loss in the temperature at the first part of the catalytic bed under traditional thermal catalysis is due to the inability of the indirect boundary heating to maintain the temperature of the catalyst due to its low thermal inertia. It is worthy to note that the problem of heat transfer at a high reactant space velocity under indirect Joule heating not only happens in a laboratory setup but could also be present in

industrial plants where heat management with a high flow rate remains the most important problem to solve.

As a partial summary, we can conclude that direct heat targeted using the induction process allows us to operate the catalytic process at its kinetic limit thanks to the extremely high heat generation within the catalyst bed and its maintenance throughout the process. In addition, such heating means can be operated using renewable energy, which could also contribute to the reduction of the carbon footprint of the process compared to the traditional gas burners.

3.2.2 Influence of the reaction temperature. The influence of the reaction temperature, which is another important parameter for the reaction, was also investigated in detail. Taken into account the high stability of the catalysts in the previous section, a single batch of catalyst was used in this study for different reaction conditions in order to reduce as much as possible artifacts by using a different catalyst for each test condition. The desulfurization performance of the NMC/SiC catalyst was fully studied under conventional Joule (JH) and induction heating (IH), and the results are presented in Fig. 5. The desulfurization performance regarding H_2S conversion and sulfur selectivity of the NMC-coated catalyst remains stable as a function of time on stream for both heating processes at a reaction temperature of 210 °C. Such results confirm the high performance of nitrogen-doped species for the desulfurization process.[26] At a reaction temperature of 210 °C, the catalyst displays similar desulfurization performance, while the sulfur selectivity is higher under JH than that of IH, *e.g.*, 82% *vs.* 70%. Decreasing the reaction temperature has more impacts on the desulfurization performance of the catalyst operated under the JH mode. Indeed, at a reaction temperature of 190 °C, the H_2S conversion is almost 100% under the IH mode (Table 1), whereas it is decreased to *ca.* 87% with the JH mode, which reveals the better desulfurization performance of the NMC catalyst operated under the IH operation mode. Further decreasing the reaction from 190 °C to 180 °C leads to a more significant difference in terms of H_2S conversion; indeed, at 180 °C the H_2S conversion under the IH mode remains high at 96%, while under JH it decreases to *ca.* 75%. Both catalysts recover the initial desulfurization performance during the return tests back to 210 °C (not shown), which confirms the high stability of the catalyst as already observed in the previous section. However, the IH mode again leads to a lower sulfur selectivity, which could be attributed to the secondary reaction between the intermediate sulfur and the excess of oxygen on some local hot spots (see discussion below). The relatively low sulfur selectivity observed on the NMC/SiC catalyst operated under the IH mode, even at relatively low reaction temperature, could be explained by the fact that some hot spots could occur at the contact point between the two catalyst particles, which could be at the origin of the over oxidation to yield SO_2, especially in the presence of excess oxygen. Khattak[49] and Haneishi *et al.*[50] have reported that a hot spot could occur at the contact point of two silicon carbide spheres during microwave heating, due to the presence of a higher concentration of electromagnetic field at such point. Fig. 5B shows that at such a low reaction temperature. The sulfur selectivity under the IH mode was slightly improved and becomes close to that observed for the NMC/SiC catalyst operated at 190 °C under the JH mode. These results confirm in part the existence of a higher surface temperature on the NMC/SiC catalyst operated under the IH mode, as suggested above. Such a high microscopic local surface temperature of the NMC/SiC catalyst under the IH mode could thus explain the higher desulfurization performance of the catalyst than that observed for the same under the JH mode.

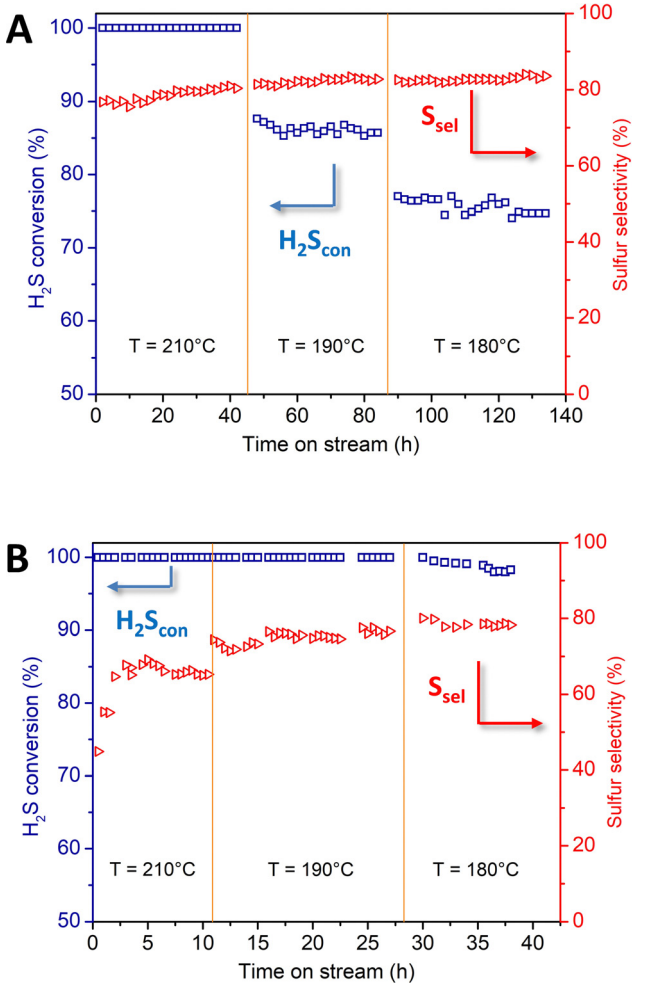

Fig. 5 Desulfurization performance on NMC/SiC operated under (A) JH and (B) IH modes. Reaction conditions: $[H_2S]$ = 1 vol%, $[O_2]$ = 2.5 vol%, $[H_2O]$ = 30 vol%, He (balance), O_2-to-H_2S ratio = 2.5, 6.0 g NMC/SiC ($V_{cat.}$ ~ 7.5 cm^3) and GHSV (STP) of 2400 h^{-1}.

Such local high temperatures can operate without changing the macroscopic temperature of the whole catalyst, as reported previously by Chaudret and co-workers during oxygen evolution reactions and hydrodeoxygenation processes.[9] In fact, the authors have achieved high catalytic performance *via* overheating the surface of the nano-catalyst, *i.e.*, FeNi nanoparticles, which induces an increase in local high temperatures well above the boiling point of the solvent in which the reaction takes place. The heat generated at such local high temperature

Table 1 Catalytic performance of different carbon-based materials for H_2S oxidation

Catalysts	Feed composition (%)	O_2/H_2S ratio	T (°C)	H_2S conv. (%)	S sel. (%)	Ref.
CNT	$H_2S/O_2/N_2$ (balance) = 0.5/0.25/99.25 (wt%)	0.5	210	27	67	17
NPC-8	H_2S/O_2 = 1.2/1.8, H_2O 30 vol% (He balance)	1.5	190	95	83	21
EM-2-800	H_2S/O_2 = 1/2.5, H_2O 30 vol%, He balance	2.5	190	100	72	22
AC	$H_2S/O_2/N_2$ (balance) = 0.5/0.25/99.25 (wt%)	0.5	200	45	100	24
N-$CNT_{2.6N}$	H_2S/O_2 = 1/2.5, H_2O 30 vol%, He balance	2.5	190	91	75	26
N@CF-800	H_2S/O_2 = 1/2.5, H_2O 30 vol%, He balance	2.5	230	57	95	27
^{A}N@C/SiC_E^2[II]	H_2S/O_2 = 1/2.5, H_2O 30 vol%, He balance	2.5	190	86	78	31
O-CNT-250-24	H_2S/O_2 = 1/2.5, H_2O 30 vol%, He balance	2.5	190	50	90	32
			210	80	88	32
N–C/CNT_{800}^{450}	H_2S/O_2 = 1/2.5, H_2O 30 vol%, He balance	2.5	190	99	79	33
		1.5	190	98	87	33
N–C/CNT-2%P	H_2S/O_2 = 1/2.5, H_2O 30 vol%, He balance	2.5	210	99	82	34
O–CNT@O-CF	H_2S/O_2 = 1/2.5, H_2O 30 vol%, He balance	2.5	200	86	86	36
			210	98	84	36
N–C/SiC	H_2S/O_2 = 1/2.5, H_2O 30 vol%, He balance	2.5	210	100	60	42
NPC700	H_2S/O_2 = 1/2.5, H_2O 30 vol%, He balance	2.5	190	97	84	46
			210	100	81	46
N-OMC-900	$H_2S/O_2/N_2$ = 0.5/0.25/99.25 (wt%), H_2O 23.5 vol%	0.5	210	75	97	55
g-C_3N_4		0.5	210	32	36	55
NMC/SiC	H_2S/O_2 = 1/2.5, H_2O 30 vol% (He balance)	2.5	180	99	79	This work
		2.5	190	100	77	
		0.63	210	99	88	

was rapidly dissipated into the whole catalyst matrix and the reactions are completed despite the relatively mild reaction conditions as measured macroscopically.

The decrease in H_2S conversion observed at 180 °C could be attributed to some sulfur deposition on the catalyst surface at this low reaction temperature, which hinders the access of the active site for the reactant. The SEM micrographs of the spent catalyst after the reaction at 180 °C were investigated. The SEM micrographs (Fig. 6) evidence the presence of sulfur particles on the catalyst surface. However, it is expected that the presence of some smaller sulfur particles, which could partially block the pore entrance of the catalyst, cannot be accurately detected by SEM analysis.

3.2.3 Influence of the O_2-to-H_2S ratio. The performance of this catalyst was further evaluated at different O_2-to-H_2S ratios with both IH and JH modes (Fig. 7). The desulfurization performance obtained with an O_2-to-H_2S ratio of 0.63 is comparable with that obtained at a ratio of 2.5 at a GHSV of 2400 h^{-1} and 210 °C (Table 1). These results indicate again the high stability of the metal-free NMC catalyst, regardless of

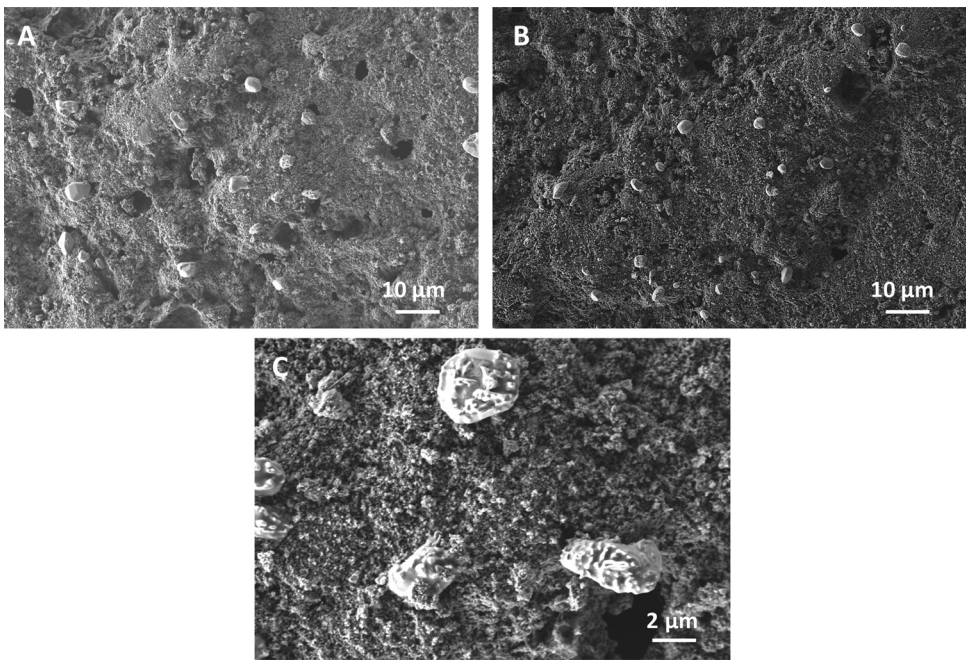

Fig. 6 (A and B) SEM micrographs of the spent NMC/SiC catalyst after the desulfurization test at 180 °C for 24 h under the IH mode showing the presence of some large discrete sulfur particles. (C) High-resolution SEM micrograph of the sulfur particles with round-shaped morphology.

the heating mode, compared to the traditional Fe-based silica catalyst, as reported in our previous articles.[31,41,51,52] The latter generally displays a noticeable deactivation with the fluctuation of the O_2-to-H_2S ratio due to the formation of iron sulphide with a lower intrinsic desulfurization activity.[53,54] The sulfur selectivity reaches the highest value at an O_2-to-H_2S ratio of 0.63, which is attributed to the self-inhibition of the secondary reaction, *i.e.*, $S + O_2 \rightarrow SO_2$, due to the lower oxygen concentration in the feedstock, and thus, the oxygen available on the catalyst surface for performing over oxidation process. Indeed, under this condition, the sulfur selectivity is directly controlled by the availability of oxygen near the active site rather by the catalyst surface temperature, as observed in the above-mentioned experiments. The sulfur selectivity is slightly lower under the IH mode at an O_2-to-H_2S ratio >0.63, while it becomes close to that obtained under the JH mode at a stoichiometric ratio. Under stoichiometric conditions, the H_2S conversion remains slightly higher under the IH mode than under the JH mode, which could be again explained by the better temperature management of the catalyst under IH.

3.2.4 Long-term stability of the NMC/SiC catalyst. For industrial implementation, the resistance towards deactivation is one of the most important parameters, as it determines the operation duration of the catalyst that will have a significant impact from both economic and environmental point of view for the process. The catalyst was also evaluated for long-term tests, *i.e.*, low temperatures, 190 °C and high GHSV, 2400 h^{-1} (Fig. 8). The results clearly indicated the high stability of the catalyst under harsh reaction conditions. This could be due to the combination of the high stability of nitrogen-doped sites incorporated within the carbon matrix with high thermal conductivity along the film, the high thermal conductivity and chemical inertness of the SiC support that allow the heat transfer in a homogeneous manner within the catalyst bed, as well as the fast and efficient heat targeting of the IH mode. Such high stability of the nitrogen-doped carbon sites has already been widely reported in our previous studies for use as a metal-free catalyst or non-innocent glue for different reaction processes under indirect Joule heating, *e.g.*, sour gas desulfurization (at higher reaction temperature) and ethylbenzene dehydrogenation.[31,40–42] The slight deactivation observed at 190 °C and 2400 h^{-1}, *i.e.*, H_2S conversion passing from 100% to 98% after *ca.* 80 h of reaction, could be attributed to the high sulfur formation rate, which cannot be efficiently removed from the catalyst surface, and thus, progressively block the access to the active sites. Such slightly deactivated catalyst can be easily recovered by subjecting the spent catalyst to thermal treatment under inert gas at 300 °C for a short period to vaporize the solid sulfur deposit.

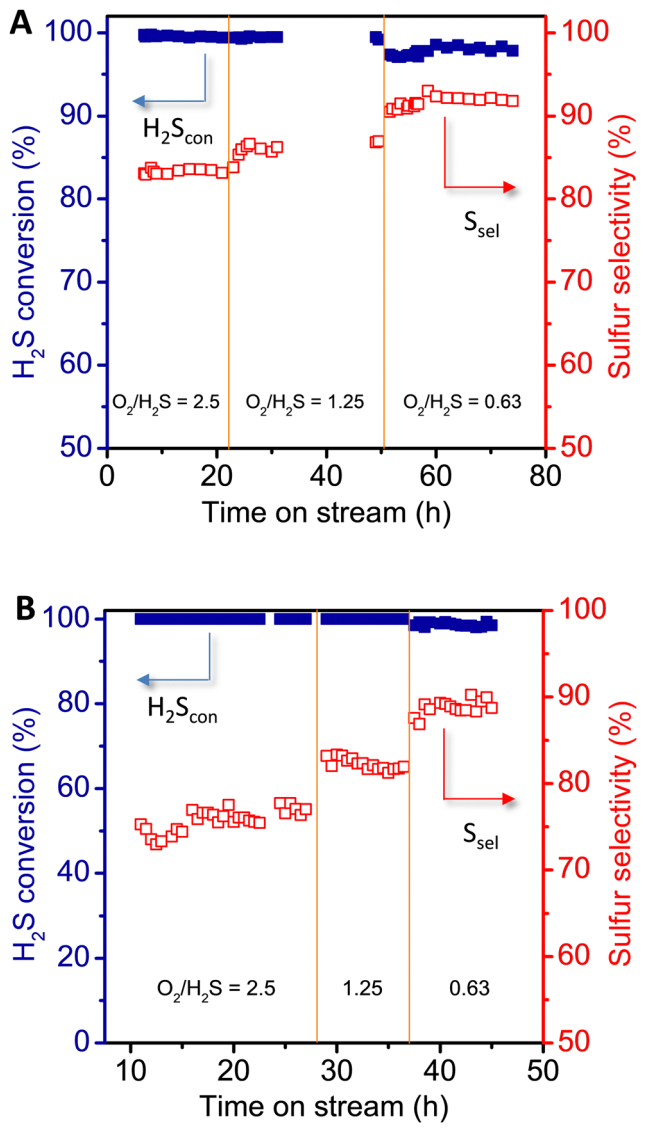

Fig. 7 Desulfurization performance on NMC/SiC operated under (A) JH and (B) IH modes. Reaction conditions: $[H_2S]$ = 1 vol%, $[H_2O]$ = 30 vol%, He (balance), 6.0 g NMC/SiC ($V_{cat.}$ ~ 7.5 cm^3), 210 °C and GHSV (STP) of 2400 h^{-1}.

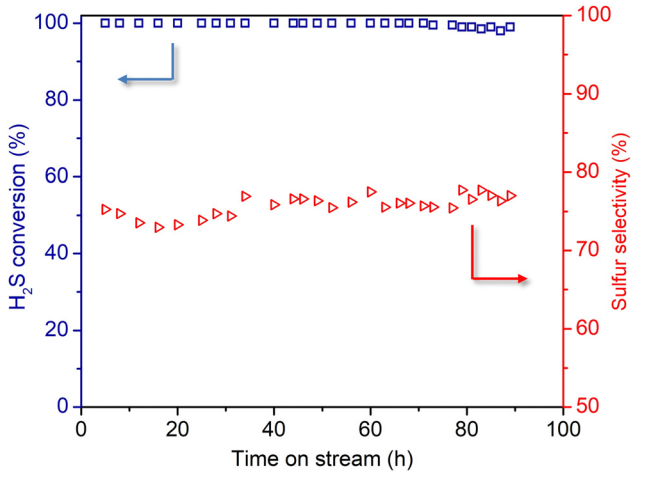

Fig. 8 Long-term desulfurization test on NMC/SiC operated under direct IH. Reaction conditions: $[H_2S]$ = 1 vol%, $[O_2]$ = 2.5 vol%, O_2-to-H_2S ratio = 2.5, $[H_2O]$ = 30 vol%, He (balance), 6.0 g NMC/SiC ($V_{cat.}$ ~ 7.5 cm^3), 190 °C and GHSV (STP) of 2400 h^{-1}.

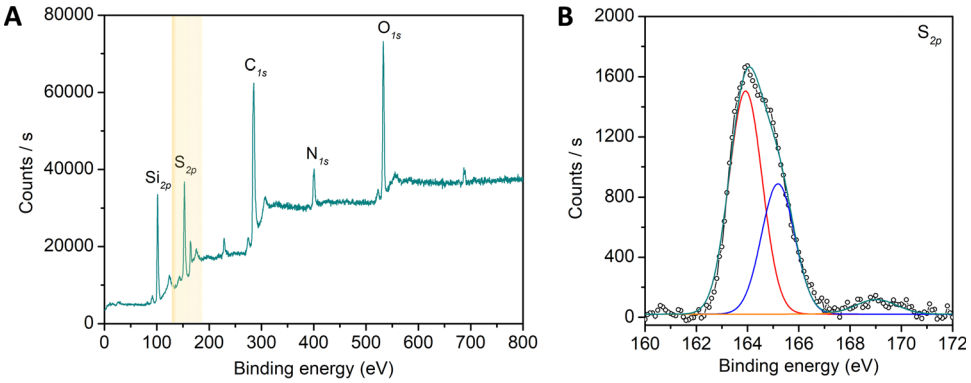

Fig. 9 XPS survey and S 2p spectra of the spent catalyst showing the presence of sulphur deposit on the surface.

The physical characteristics, *e.g.*, SSA and pore size distribution, of the spent NMC/SiC catalyst after long-term evaluation were analyzed and compared with those of the pristine catalyst: the pristine catalyst shows an SSA of 54 $m^2\ g^{-1}$, while the spent catalyst displays an SSA of 14 $m^2\ g^{-1}$. The loss of the SSA of the spent catalyst could be attributed in part to the solid sulfur deposition, as discussed in the previous section. The decrease in the SSA is also accompanied by a disappearance of small pores, *i.e.*, 2 nm, and a contribution of mesopore centered at around 8.0 ± 1 nm. The XPS analysis of the spent catalyst reveals the presence of a S 1s peak, which confirms the presence of some solid sulfur deposited during the reaction on the surface of the catalyst (Fig. 9). It is expected that such sulfur deposit could partially block the access of the reactant to the active site. However, it is worthy to note that the long-term reaction was carried out under drastic conditions, *i.e.*, low temperatures (which favors the sulfur deposit) and a high space velocity, and thus, to avoid such slight deactivation, the process should take place at a higher reaction temperature in order to avoid residual sulfur deposit. It is worthy to note that despite the significant SSA loss, the desulfurization activity remains extremely stable, which confirms the high performance of the layered NMC/SiC catalyst.

4. Conclusion

In summary, a combination of a silicon carbide catalyst (NMC/SiC) coated with thin-layer nitrogen-doped mesoporous carbon, with high thermal conductivity, and contactless induction heating displayed high efficiency for performing the selective oxidation of H_2S under different conditions. The IH displays several advantages for operating the catalytic desulfurization process under severe reaction conditions compared with traditional JH, *i.e.*, easily operate catalytic desulfurization process with good performance at a much lower temperature (180 °C) and a higher GHSV (3600 h^{-1}). Heat was directly targeted to the solid catalyst/susceptor, while the entrance gas was not heated, which contributed to the reduction of the overall energy input compared to the traditional indirect convection/conduction heating where significant heat was lost *via* convection and conduction processes from the oven to the catalyst bed. The harvested heat was rapidly transferred through the layer of NMC with high heat conductivity to the entire surface of the catalyst where the reaction takes place. In addition, the high heat targeting of the contactless induction heating allows the fast temperature regulation of the catalyst, which could efficiently off-set the large heat loss *via* gas–solid heat exchange when operated at a high space velocity as encountered with traditional Joule heating. The current study also opens up the possibility of integrating the IH system into renewable energy networks. As a plug-and-play small and highly efficient system, IH could contribute to the decentralization of industrial units to the extraction place and significantly reduce the overall carbon footprint of the process by reducing the energy cost associated with transport over long distances.

Author contributions

W. Wang: methodology, data acquisition, experiments, writing. C. Duong-Viet: methodology, data acquisition, experiments, experimental discussion, writing. L. Truong-Phuoc: data acquisition, experiments. L. Nguyen-Dinh: experimental discussion, formal analysis, writing. H. M. Nguyen: experimental discussion, formal analysis, writing. Y. Liu: experimental discussion, writing, funding, supervision. C. Pham-Huu: experimental discussion, writing, funding, supervision.

Conflicts of interest

The authors declare that they have no known competing financial interests or personal relationships that could have appeared to influence the work reported in this paper.

Acknowledgements

C. D. V., T. T.-H., L. N. D. and C. P.-H. would like to thank the Vietnam National Foundation for Science and Technology Development (NAFOSTED) for financial support under grant number 104.05-2017.336. W. W. would like to thank the China Scholarship Council (CSC) for financial support during his PhD stay at the ICPEES. Y. L. would like also to thank the financially supported from the NSFC of China (21606243), CAS Youth

Innovation Promotion Association (2018220) and Liao Ning Revitalization Talents Program (XLYC1907053). SICAT SARL (www.sicatcatalyst.com) is gratefully acknowledged for providing SiC foam samples. Dr Ch. Pham (www.sicatcalyst.com) is gratefully acknowledged for providing SiC sample for the experiments and for helpful discussion. The SEM analysis was carried out at the SEM platform of the ICPEES-IPCMS and T. Romero (ICPEES) is gratefully acknowledged. The TEM analysis was carried out at the DICP TEM platform facilities.

References

1 F. Wang, J. D. Harindintwali, Z. Yuan, M. Wang, F. Wang, S. Li, Z. Yin, L. Huang, Y. Fu, L. Li, S. X. Chang, L. Zhang, J. Rinklebe, Z. Yuan, Q. Zhu, L. Xiang, D. C. W. Tsang, L. Xu, X. Li, W. Chen, N. Jiao, J. Lehmann, Y.-G. Zhu, H. Jin, A. Schäffer, J. M. Tiedje and J. M. Chen, *Innovation*, 2021, **2**(4), 100180.

2 T. Xiao, T. Shirvani, O. Inderwildi, S. Gonzalez-Cortes, H. AlMegren, D. King and P. P. Edwards, *Top. Catal.*, 2015, **58**(10), 682–695.

3 V. Rudnev, D. Loveless and R. L. Cook, *Handbook of Induction Heating*, CRC Press, Boca Raton, FL, 2017.

4 O. Lucía, P. Maussion, E. J. Dede and J. M. Burdío, *IEEE Trans. Ind. Electron.*, 2013, **61**(5), 2509–2520.

5 R. Piner, H. Li, X. Kong, L. Tao, I. N. Kholmanov, H. Ji, W. H. Lee, J. W. Suk, J. Ye, Y. Hao, S. Chen, C. W. Magnuson, A. F. Ismach, D. Akinwande and R. S. Ruoff, *ACS Nano*, 2013, **7**(9), 7495–7499.

6 W. Wang, G. Tuci, C. Duong-Viet, Y. Liu, A. Rossin, L. Luconi, J.-M. Nhut, L. Nguyen-Dinh, C. Pham-Huu and G. Giambastiani, *ACS Catal.*, 2019, **9**, 7921–7935.

7 H. Kreissl, J. Jin, S. H. Lin, D. Schüette, S. Störtte, N. Levin, B. Chaudret, A. J. Vorholt, A. Bordet and W. Leitner, *Angew. Chem., Int. Ed.*, 2021, **60**, 26639–26646.

8 C. Cerezo-Navarrete, I. M. Marin, H. García-Miquel, A. Corma, B. Chaudret and L. M. Martínez-Prieto, *ACS Catal.*, 2022, **12**, 8462–8475.

9 I. M. Marin, D. De Masi, L. M. Lacroix, P. F. Fazzini, P. W. van Leeuwen, J. M. Asensio and B. Chaudret, *Green Chem.*, 2021, **23**(5), 2025–2036.

10 L. Truong-Phuoc, C. Duong-Viet, G. Tuci, A. Rossin, J. M. Nhut, W. Baaziz, O. Ersen, M. Arab, A. Jourdan, G. Giambastiani, C. Pham-Huu and A. C. S. Sustainable, *Chem. Eng.*, 2022, **10**(1), 622–632.

11 C. Niether, S. Faure, A. Bordet, J. Deseure, M. Chatenet, J. Carrey, B. Chaudret and A. Rouet, *Nat. Energy*, 2018, **3**(6), 476–483.

12 J. Bursavich, M. Abu-Laban, P. D. Muley, D. Boldor and D. J. Hayes, *Energy Convers. Manage.*, 2019, **183**, 689–697.

13 W. Wang, C. Duong-Viet, G. Tuci, Y. Liu, A. Rossin, L. Luconi, J. M. Nhut, L. Nguyen-Dinh, G. Giambastiani and C. Pham-Huu, *ChemSusChem*, 2020, **13**(20), 5468–5479.

14 W. Zhao, B. Veerappan Vaithilingam, S. Ghosh, X. Li, F. Geuzebroek, A. S. El Nasr, I. Khan, S. Dara, N. Mittal, P. Daoutidis, S. Al Hashimi, K. Andre Mkhoyan, Y. Al Wahedi, M. Tsapatsis and A. Stein, *Ind. Eng. Chem. Res.*, 2021, **60**(41), 14779–14787.

15 X. Zhang, Y. Tang, S. Qu, J. Da and Z. Hao, *ACS Catal.*, 2015, **5**, 1053–1067.

16 J. Jiang, A. Chan, S. Ali, A. Saha, K. J. Haushalter, W. L. M. Lam, M. Glasheen, J. Parker, M. Brenner, S. B. Mahon, H. H. Patel, R. Ambasudhan, S. A. Lipton, R. B. Pile and G. R. Boss, *Sci. Rep.*, 2016, **6**(1), 20831.

17 C. Yang, H. Ye, J. Byun, Y. Hou and X. Wang, *Environ. Sci. Technol.*, 2020, **54**(19), 12621–12630.

18 X. Zhang, Z. Wang, N. Qiao, S. Qu and Z. Hao, *ACS Catal.*, 2014, **4**, 1500–1510.

19 X. Zheng, Y. Li, L. Zhang, L. Shen, Y. Xiao, Y. Zhang, C. Au and L. Jiang, *Appl. Catal., B*, 2019, **252**, 98–110.

20 L. Shen, X. Zheng, G. Lei, X. Li, Y. Cao and L. Jiang, *Chem. Eng. J.*, 2018, **346**, 238–248.

21 X. Zhang, C. Xu, S. Li, X. Liu and Y. Liu, *Appl. Mater. Today*, 2021, **25**, 101228.

22 S. Li, Q. Gu, N. Cao, Q. Jiang, C. Xu, C. Jiang, C. Chen, C. Pham-Huu and Y. Liu, *J. Mater. Chem. A*, 2020, **8**(18), 8892–8902.

23 Z. Yu, X. Wang, Y. N. Hou, X. Pan, Z. Zhao and J. Qiu, *Carbon*, 2017, **117**, 376–382.

24 X. Kan, X. Chen, W. Chen, J. Mi, J.-Y. Zhang, F. Liu, A. Zheng, K. Huang, L. Shen, C. Au and L. Jiang, *Chem. Eng.*, 2019, **7**, 7609–7618.

25 M. Sun, X. Wang, X. Pan, L. Liu, Y. Li, Z. Zhao and J. Qiu, *Fuel Process. Technol.*, 2019, **191**, 121–128.

26 K. Chizari, A. Deneuve, O. Ersen, I. Florea, Y. Liu, D. Edouard, I. Janowska, D. Begin and C. Pham-Huu, *ChemSusChem*, 2012, **5**, 102–108.

27 Y. Liu, C. Duong-Viet, J. Luo, A. Hébraud, G. Schlatter, O. Ersen, J. M. Nhut and C. Pham-Huu, *ChemCatChem*, 2015, **7**, 2957–2964.

28 Z. Zhang, W. Jiang, D. Long, J. Wang, W. Qiao and L. Ling, *ACS Appl. Mater. Interfaces*, 2017, **9**(3), 2477–2484.

29 Q. Chen, Z. Wang, D. Long, X. Liu, L. Zhan, X. Liang, W. Qiao and L. Ling, *Ind. Eng. Chem. Res.*, 2010, **49**, 3152–3159.

30 Z. Zhang, J. Wang, W. Li, M. Wang, W. Qiao, D. Long and L. Ling, *Carbon*, 2016, **96**, 608–615.

31 H. Ba, Y. Liu, L. Truong-Phuoc, C. Duong-Viet, X. Mu, W. H. Doh, T. Tran-Thanh, W. Baaziz, L. Nguyen-Dinh, J.-M. Nhut, I. Janowska, D. Begin, S. Zafeiratos, P. Granger, G. Tuci, G. Giambastiani, F. Banhart, M. J. Ledoux and C. Pham-Huu, *Chem. Commun.*, 2015, **51**, 14393–14396.

32 C. Duong-Viet, Y. Liu, H. Ba, L. Truong-Phuoc, W. Baaziz, L. Nguyen-Dinh, J.-M. Nhut and C. Pham-Huu, *Appl. Catal., B*, 2016, **191**, 29–41.

33 S. Li, Y. Liu, H. Gong, K.-H. Wu, H. Ba, C. Duong-Viet, C. Jiang, C. Pham-Huu and D. Su, *ACS Appl. Nano Mater.*, 2019, **2**, 3780–3792.

34 C. Xu, Q. Gu, S. Li, J. Ma, Y. Zhou, X. Zhang, C. Jiang, C. Pham-Huu and Y. Liu, *ACS Catal.*, 2021, **11**, 8591–8604.

35 W. Wang, C. Duong-Viet, Z. Xu, H. Ba, G. Tuci, G. Giambastiani, Y. Liu, T. Truong-Huu, J. M. Nhut and C. Pham-Huu, *Catal. Today*, 2020, **357**, 214–220.

36 T. Truong-Huu, C. Duong-Viet, H. Duong-The, J.-M. Nhut, T. Romero, L. Truong-Phuoc, H. Ba, L. Nguyen-Dinh and C. Pham-Huu, *Appl. Catal., A*, 2021, **620**, 118171.
37 G. Tuci, Y. Liu, A. Rossin, X. Guo, C. Pham, G. Giambastiani and C. Pham-Huu, *Chem. Rev.*, 2021, **121**, 10559–10665.
38 S. R. Kulkarni, V. K. Velisoju, F. Tavares, A. Dikhtiarenko, J. Gascon and P. Castaño, *Catal. Rev.*, 2022, 1–64.
39 P. Nguyen and C. Pham, *Appl. Catal., A*, 2011, **391**(1–2), 443–454.
40 H. Ba, J. Luo, Y. Liu, C. Duong-Viet, G. Tuci, G. Giambastiani, J.-M. Nhut, L. Nguyen-Dinh, O. Ersen and D. S. Su, *Appl. Catal., B*, 2017, **200**, 343–350.
41 Y. Liu, H. Ba, J. Luo, K.-H. Wu, J.-M. Nhut, D. S. Su and C. Pham-Huu, *Catal. Today*, 2018, **301**, 38–47.
42 C. Duong-Viet, J.-M. Nhut, T. Truong-Huu, G. Tuci, L. Nguyen-Dinh, Y. Liu, C. Pham, G. Giambastiani and C. Pham-Huu, *Catal. Sci. Technol.*, 2020, **10**, 5487–5500.
43 P. Leroi, B. Madani, C. Pham-Huu, M.-J. Ledoux, S. Savin-Poncet and J. L. Bousquet, *Catal. Today*, 2004, **91**, 53–58.
44 E. D. Mantiply, K. R. Pohl, S. W. Poppell and J. A. Murphy, *Bioelectromagnetics*, 1997, **18**, 563–577.
45 T. Koppel, I. Vilcane and P. Tint, 16th International Scientific Conference Engineering for Rural Development, 2017.
46 C. Xu, J. Chen, S. Li, Q. Gu, D. Wang, C. Jiang and Y. Liu, *J. Hazard. Mater.*, 2021, **403**, 123806.
47 A. Malhotra, W. Chen, H. Goyal, P. J. Plaza-Gonzalez, I. Julian, J. M. Catala-Civera and D. G. Vlachos, *Ind. Eng. Chem. Res.*, 2021, **60**, 6835–6847.
48 I. Julian, H. Ramirez, J. L. Hueso, R. Mallada and J. Santamaria, *Chem. Eng. J.*, 2019, **377**, 119764.
49 H. K. Khattak, P. Banucc and A. D. Slepkov, *Proc. Natl. Acad. Sci. U. S. A.*, 2019, **116**(10), 4000–4005.
50 N. Haneishi, S. Tsubaki, E. Abe, M. M. Maitani, E. Suzuki, S. Fujii, J. Fukushima, H. Takizawa and Y. Wada, *Sci. Rep.*, 2019, **9**, 222.
51 N. Keller, C. Pham-Huu and M. J. Ledoux, *Appl. Catal., A*, 2001, **217**(1–2), 205–217.
52 P. Nguyen, J. M. Nhut, D. Edouard, C. Pham, M. J. Ledoux and C. Pham-Huu, *Catal. Today*, 2009, **141**(3–4), 397–402.
53 X. Zhang, G. Dou, Z. Wang, L. Li, Y. Wang, H. Wang and Z. Hao, *J. Hazard. Mater.*, 2013, **260**, 104–111.
54 X. Yao, J. Xu, Z. Hong, G. Li, X. Wang, F. Lu, W. Wang, H. Liu, C. Liang and Z. Lin, *J. Phys. Chem. C*, 2018, **122**, 3263–3272.
55 S. Liang, J. Mi, F. Liu, Y. Zheng, Y. Xiao, Y. Cao and L. Jiang, *Chem. Eng. Sci.*, 2020, **221**, 115714.

